

Investigation of the Jets of the Blazar 3C 279 with Korean VLBI Network (KVN) 22–129 GHz Observations

Sungmin Yoo¹, Sang-Sung Lee^{2,3}, Sang-Hyun Kim^{2,3}, Hongjun An^{1†}

¹Department of Astronomy and Space Sciences, Chungbuk National University, Cheongju 28644, Korea

²Korea Astronomy and Space Science Institute, Daejeon 34055, Korea

³Astronomy and Space Science, University of Science and Technology, Daejeon 34113, Korea

We present analysis results of Korean VLBI Network (KVN) four-band data for the highly variable blazar 3C 279. We measured the 22, 43, 86, and 129 GHz flux densities and spectral indices of the source using contemporaneous data taken over 5.6 years. We used the discrete correlation function to investigate correlations between the radio emission properties and those measured in the optical ($2 \times 10^{14} - 1.5 \times 10^{15}$ Hz), X-ray (0.3–10 keV), and gamma-ray (0.1–300 GeV) bands. We found a significant correlation between the radio spectral index and gamma-ray flux without a time delay and interpreted the correlation using an extended jet scenario for blazar emission.

Keywords: blazar (3C 279), relativistic jets, synchrotron self-absorption (SSA), variability

1. INTRODUCTION

Active galactic nuclei (AGNs) are compact regions at the center of galaxies that consist of a supermassive black hole, bipolar jets, a surrounding accretion disk and dusty torus, and line-emitting regions (Blandford et al. 2019). AGNs having a jet that is aligned with Earth's line of sight are called blazars (Urry & Padovani 1995). The jets, which are powered by accretion onto and/or the rotation of the central black hole (Blandford & Znajek 1977; Blandford & Payne 1982), carry enormous amounts of energy; thus, particles in the jets are very energetic. Consequently, it is thought that AGN jets can affect the evolution of the universe and be a primary source of ultrahigh-energy cosmic rays (UHECRs) detected on Earth (Murase et al. 2012). Moreover, these jets enable the study of the environment in the early universe (e.g., Ackermann et al. 2016; An & Romani 2018, 2020). To further our understanding of the universe and UHECRs, we need to understand these jets in detail. However, the components of the jets (e.g., the magnetic field B and

particle species) and the acceleration and flow of particles in the jets are not yet well understood.

It is well known that AGN jets are extended (even beyond the kiloparsec scale) and emit radiation in broad wavebands. The broadband emission exhibits complex variability: correlated variability in multiple wavebands (e.g., Hodgson et al. 2018), orphan flares in one waveband (e.g., MacDonald et al. 2017), and time-delayed correlation between the variabilities in multiple wavebands (e.g., Larionov et al. 2020). The observed complexity is related to the emission mechanism, jet flow structure, and propagation of disturbances in the jet (e.g., Sokolov et al. 2004; Rieger & Aharonian 2012). An extended jet scenario is often used to explain the complexity, where particle cooling and the synchrotron self-absorption (SSA; Türler et al. 2000) effect significantly influence the observed emission (e.g., Rieger & Aharonian 2012).

In the extended jet scenario, high-energy particles are injected into the inner region of the jet (near the black hole) and propagate along the jet to the outer region. In the inner

© This is an Open Access article distributed under the terms of the Creative Commons Attribution Non-Commercial License (<https://creativecommons.org/licenses/by-nc/3.0/>) which permits unrestricted non-commercial use, distribution, and reproduction in any medium, provided the original work is properly cited.

Received 02 JUN 2021 Revised 28 OCT 2021 Accepted 02 NOV 2021

† Corresponding Author

Tel: +82-43-261-2314, E-mail: hjan@cbnu.ac.kr

ORCID: <https://orcid.org/0000-0002-6389-9012>

region, high-frequency radiation is emitted by energetic (freshly injected) particles, and low-frequency radiation is attenuated by SSA. The particles lose energy via radiation; thus, their emission frequencies decrease with increasing distance from the black hole. This phenomenon is called frequency or longitudinal stratification of the jet (e.g., Rieger & Aharonian 2012). If an event such as sudden particle injection or the formation of a shock occurs in a region of the jet, a signature of the event (e.g., flaring activity) is observed first in the high-energy emission and then in the low-energy emission when the event propagates to the outer region. This scenario can be tested using multiband spectral correlation studies.

3C 279 is a bright blazar with a redshift of 0.5362 (Marziani et al. 1996). The source has been monitored for a long time (e.g., Lee et al. 2016; Lister et al. 2018), and its light curves show complex variability (e.g., Rani et al. 2017) with minute-scale gamma-ray flares (e.g., Hayashida et al. 2015) and long- (> 1,000 d) and short-term (~100 d) radio activity (e.g., Hovatta et al. 2008; Larionov et al. 2020). Studies using polarimetric and interferometric data have revealed various phenomena (e.g., polarization swing and jet bending; Kiehlmann et al. 2016; Kim et al. 2020) associated with multifrequency activity that provided information about the source. However, these observed properties of the source are too complex for the limited observational data and analyses to fully address. Therefore, further studies are needed.

In this study, we used contemporaneous radio observations taken with the Korean VLBI Network (KVN) (e.g., Lee et

al. 2014) at 22, 43, 86, and 129 GHz to study the jet of 3C 279. We measured the radio spectral properties and their variation using KVN VLBI data taken over ~5.6 years, from MJD 56265 (December 4, 2012) to MJD 58270 (June 1, 2018). We compared the radio and high-energy spectral properties to investigate the relationship between the low-energy and high-energy emission zones in the extended jet. We describe the data reduction processes in Section 2, present the analysis results in Section 3, and interpret the results using an extended jet scenario in Section 4.

2. DATA REDUCTION

We used four-band (22, 43, 86, and 129 GHz) contemporaneous radio observations of 3C 279 by the KVN between MJD 56265 (December 4, 2012) and MJD 58270 (June 1, 2018). Observations were taken with a 30-d cadence (except for maintenance periods) in the interferometric configuration (Lee et al. 2016), and the observational data were reduced using the KVN pipeline (Hodgson et al. 2016). We conducted an imaging process using the CLEAN algorithm (Högbom 1974); we fit the VLBI image (dirty map) with a model having a source component and gradually added more components until the residual level converged. This process provided CLEAN images (Fig. 1, left). We then inspected the reliability of the CLEAN images using imaging parameters (e.g., residual noise; Fig. 1, right) and discarded data with an unreliable CLEAN image.

We estimated the quality of the cleaning process using

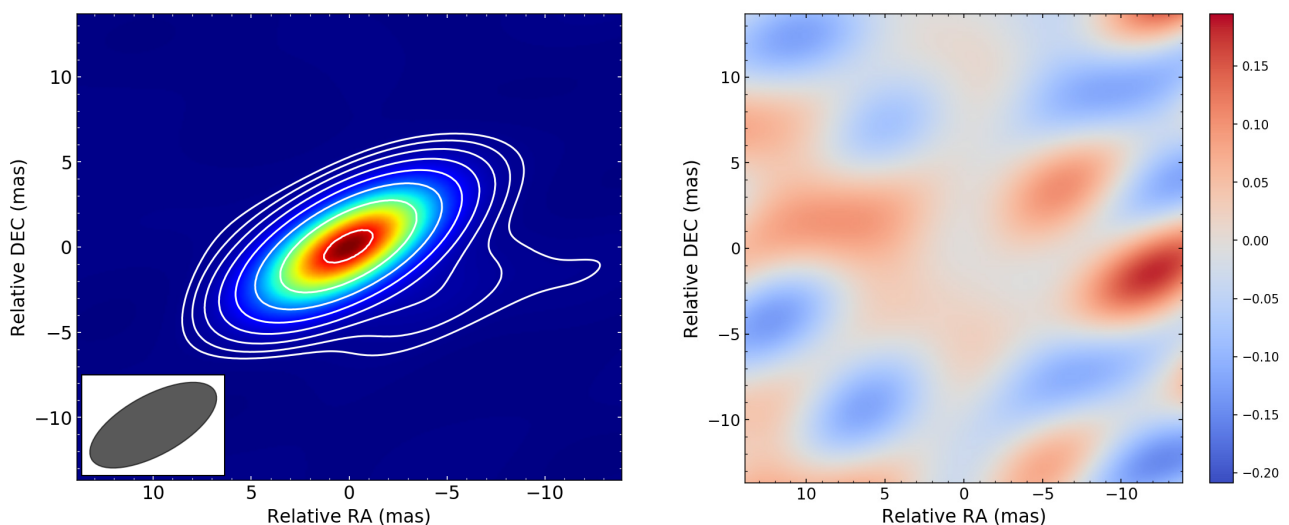


Fig. 1. A CLEAN image (left) and residual map (right) made with a 22 GHz radio VLBI observation obtained with KVN on MJD 56350 (2013 February 27). The peak flux density of the CLEAN image (left) is $25.4 \text{ Jy beam}^{-1}$, and we show 8 logarithmically spaced contours between 1% and 90% of the peak value. The small ellipse ($7.47 \times 3.38 \text{ mas}$ with a position angle of -56°) in the lower left corner of the left panel is the beam size for the observation. KVN, Korean VLBI Network.

the image quality factor ϵ_r , which is the ratio of the measured and expected maximum flux densities in the residual image, and was used to calculate $\kappa_\sigma = \exp(|\ln \epsilon_r|) - 1$ (Lobanov et al. 2006). A small value of κ_σ (e.g., < 1) indicates that the residual follows a Gaussian distribution and that the model represents the data well (Lee et al. 2016). A CLEAN image and residual map are shown in Fig. 1. We followed this procedure for each observation and obtained an average κ_σ value of 0.5, which indicates that the cleaning process performed reasonably well.

We measured the source flux density by integrating the (modeled) CLEAN flux densities, most of which were from a central compact region (Fig. 1, left). The brightness decreases

very rapidly with distance from the center. Because high-energy emission is produced in a compact region (inner region), we focus on a small region and use the radio flux densities within a central $10 \times 10 \text{ mas}^2$ region to study the correlation between the radio and high-energy properties. We verified that the results presented below did not vary with the size of the region (e.g., $2 \times 2 \text{ mas}^2$, $6 \times 6 \text{ mas}^2$, or $15 \times 15 \text{ mas}^2$) or source model (e.g., delta functions or Gaussians). We assumed uncertainties of 5%, 5%, 10%, and 30% for the 22, 43, 86, and 129 GHz flux densities, respectively, as reported previously (Lee et al. 2020). The measured light curves of the four bands are shown in Fig. 2(a).

Note that the transverse physical scales considered are

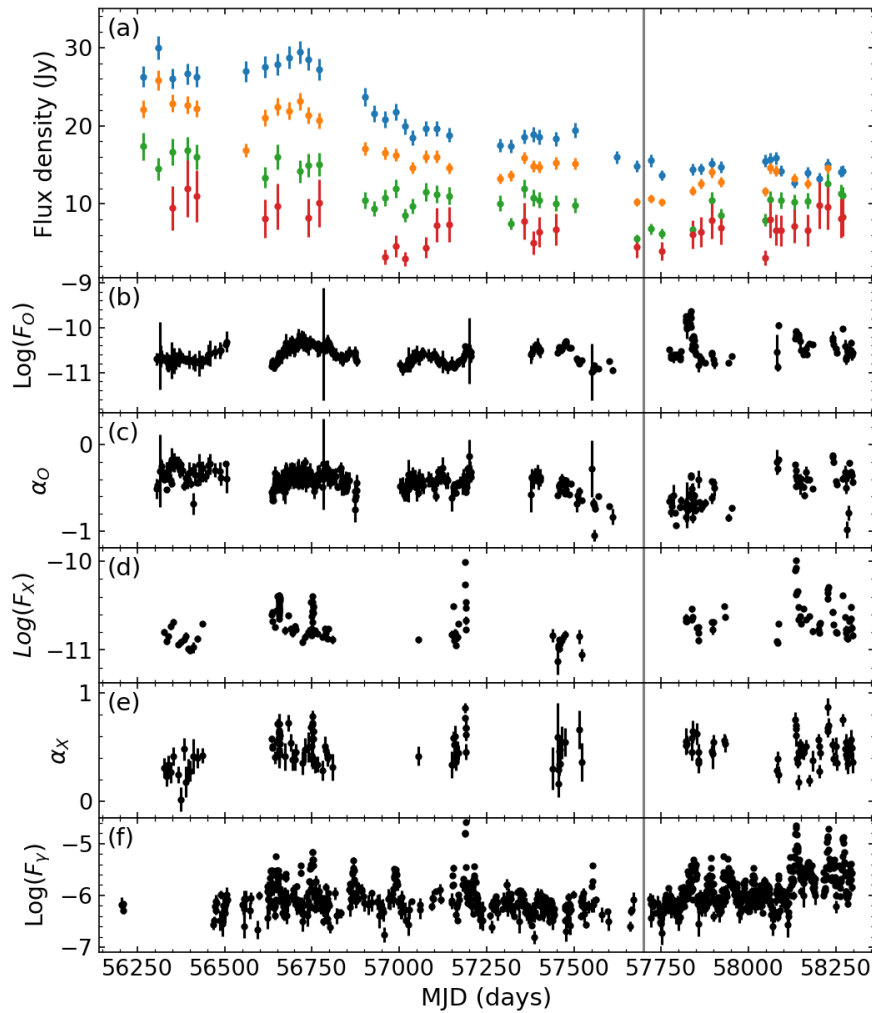


Fig. 2. Light curves and spectral indices in the radio to the gamma-ray bands measured over a period of 5.6 year from MJD 56265 (2012 December 4) to MJD 58270 (2018 June 1). (a) 22, 43, 86, and 129 GHz flux densities measured with KVN: 22 GHz (blue), 43 GHz (orange), 86 GHz (green), and 129 GHz (red). (b, c) Emission properties in the optical band: fluxes (b) and spectral indices (c). (d, e) 0.3–10 keV X-ray emission properties: fluxes (d) and spectral indices (e). (f) A 0.1–300 GeV Fermi light curve. The vertical gray line marks MJD 57700. The radio measurements are made in this work (Section 2), the optical and X-ray data are taken from literature (Yoo & An 2020), and the gamma-ray data are downloaded from the Fermi Science Support Center (FSSC). KVN, Korean VLBI Network.

rather large (e.g., ~10 pc for the smallest region). Because high-energy emission is thought to be produced in a very compact region (e.g., < 1 pc), it is desirable to use a comparable (or slightly larger) radio region. Resolving such a small region is impossible using our data (even if we use higher-resolution VLBI data); therefore, our radio measurements include emission from large-scale regions. The large-scale emission may blur the radio/high-energy correlation below (Section 3.2). However, as noted above, the radio brightness decreases quite rapidly with distance; thus, the blur might not be very severe.

Note that the KVN VLBI data provide four-band images with modest angular resolution. We inspected our images for any noticeable features that may be related to high-energy activity, but we did not find any. Therefore, we do not present detailed image analysis results but focus on contemporaneous broadband (22–129 GHz) radio spectral variability in this paper. Note, however, that higher-resolution (0.2 mas) radio images of 3C 279 showed features that might be related to high-energy activity (e.g., Larionov et al. 2020).

The high-energy data were published results (Figs. 2(b)–2(e)) in the optical and X-ray bands from Steward, SMART, and Swift/UVOT (optical band) and Swift/XRT data (Yoo & An 2020). The optical-band spectral index α_0 and flux F_0 were measured in the $2 \times 10^{14} - 1.5 \times 10^{15}$ Hz band, and the X-ray band spectral properties (α_x and F_x) were measured in the 0.3–10 keV band. The gamma-ray data are the daily light curve (0.1–300 GeV flux, F_γ ; Fig. 2(f); Fermi, 2021) measured by the Fermi Large Area Telescope in the 0.1–300 GeV band.

3. DATA ANALYSIS

3.1 Measurements of Radio Spectral Index

We first measured the radio spectral indices using radio flux density measurements (Fig. 2(a)). For a pair of flux densities (f_{ν_1} and f_{ν_2}) at two adjacent radio frequencies (ν_1 and ν_2), we computed the power-law spectral index $\alpha_{\nu_1, \nu_2} = \frac{\log f_{\nu_2} - \log f_{\nu_1}}{\log \nu_2 - \log \nu_1}$. This calculation was made for 22–43 GHz, 43–86 GHz, and 86–128 GHz pairs; the results are displayed in Figs. 3(a)–3(c). Note that the low-frequency spectral indices (α_{22-43} and α_{43-86}) seem to decrease until MJD 57700 and then increase, but the highest-frequency index (α_{86-129}) shows no apparent long-term change, indicating that the radio spectral variability was stronger in the low-frequency band. We quantify these results by fitting the temporal trends of the indices with two linear functions, one before MJD 57700 and the other after it. The best-fit functions are

shown as green and blue lines in Fig. 3, and the best-fit slopes are given in the figure. The slopes are consistent with 0 (at the $< 2\sigma$ level) before MJD 57700. After MJD 57700, the low-frequency indices, α_{22-43} and α_{43-86} , increase with a positive slope (i.e., they increase with time) at the $\geq 3\sigma$ level, whereas the slope for the highest-frequency index, α_{86-129} , remains consistent with 0. To determine whether the changes in the spectral index evolution are accompanied by a change in radio morphology, we inspected our KVN images before and after the epoch MJD 57700. The radio morphology seemed to change randomly over the observation period, and we found no systematic difference between periods before and after MJD 57700.

Next, we characterized the broadband radio emission by measuring the spectral turnover frequency. Specifically, we fit the four-band radio spectra with a log-parabolic model $F(\nu) = f_c \left(\frac{\nu}{\nu_c} \right)^{2a(1 - \nu/\nu_c)}$ (e.g., Algaba et al. 2018), where ν_c is the turnover frequency, f_c is the turnover flux density, and a is a slope parameter. Although this characterization can provide new information on the variability, the measurements have large uncertainties because we have only four-band (or three sometimes) measurements. The results are presented in Figs. 3(d) and 3(e). The temporal trend of ν_c is similar to that of α_{22-43} , decreasing before MJD 57700 and then increasing. We fit the ν_c evolution with two linear functions, as described above, and found that the slope changed from $(-1.6 \pm 4.9) \times 10^{-3} \text{ day}^{-1}$ to $(2.9 \pm 1.5) \times 10^{-2} \text{ day}^{-1}$. The change is significant at the 2σ level. Note, however, that the positive trend after MJD 57700 seems to be driven by a single point at MJD 58130; if we ignore it, the slope after MJD 57700 is consistent with 0. Moreover, the measured ν_c value is below 22 GHz, the lowest frequency of the KVN observations, in some epochs; these measurements may be less reliable. Thus, the change in the temporal trend of ν_c is less certain than those of α_{22-43} and α_{43-86} .

3.2 Discrete Correlation Function (DCF) Analysis

We first conducted a correlation study between the four-band radio flux densities and high-energy spectral properties (flux and spectral index) using the discrete correlation function (DCF) (Max-Moerbeck et al. 2014). The 22, 43, 86, and 129 GHz and turnover flux densities are cross-correlated with the high-energy properties, flux F_x , and spectral index α_x , where x is O, X, and γ for the optical, X-ray, and gamma-ray bands, respectively. For each pair, we computed the DCF on a 500-d time scale (15-d bins). The results are presented in Fig. 4, where our measurements are shown in black, and the 1σ , 2σ , and 3σ confidence intervals are denoted by red, blue, and green dotted lines,

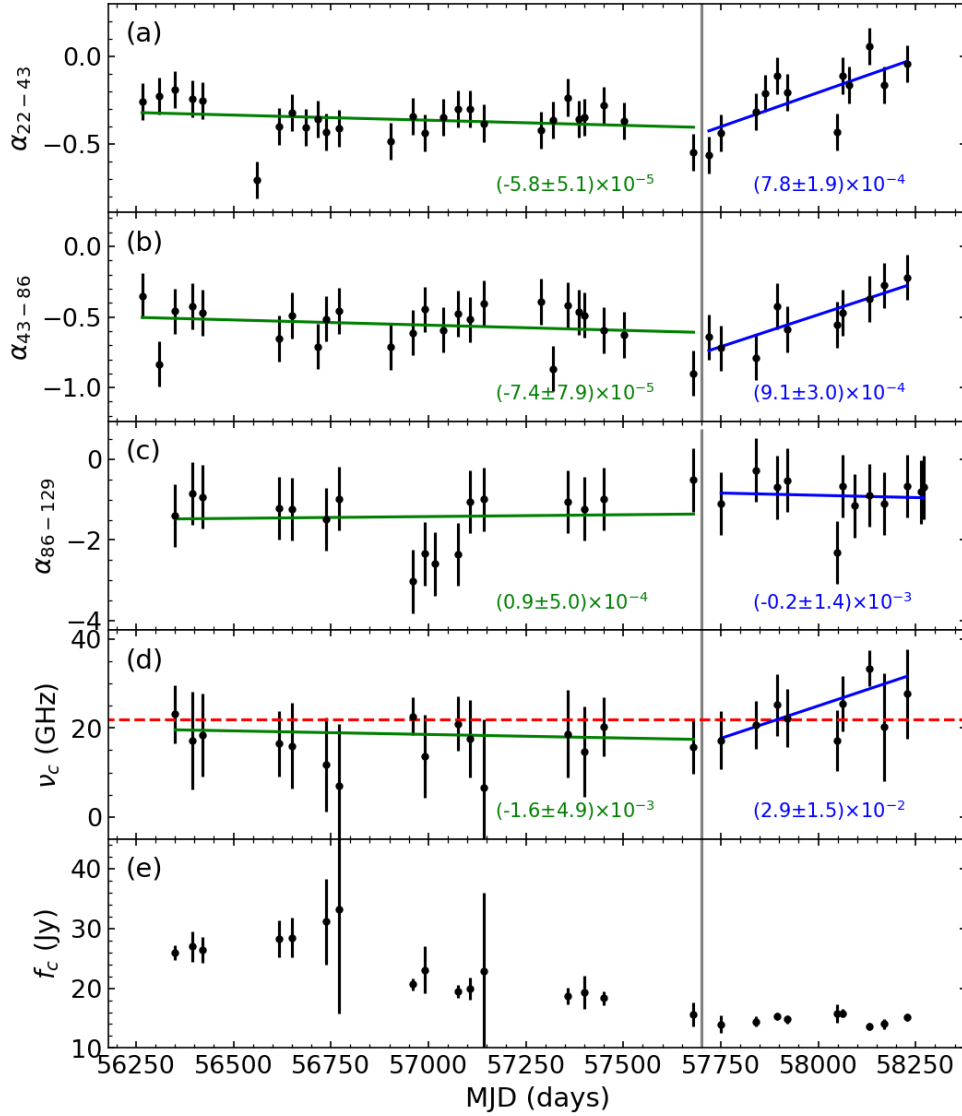


Fig. 3. Radio spectral indices and turnover frequency. (a–c) Spectral indices measured using pairs of the radio flux-density measurements (Fig. 2(a)): 22–43 GHz (α_{22-43} ; a), 43–86 GHz (α_{43-86} ; b), and 86–129 GHz (α_{86-129} ; c). (d, e) Turnover frequency (ν_c) and flux density (f_c) inferred from log-parabolic model fits (see text). Green and blue lines are the best-fit linear functions (in units of days^{-1}) for the data taken before and after MJD 57700, respectively, and the best-fit slopes of the functions are presented in the figure. The vertical line denotes MJD 57700. The horizontal line in panel (d) denotes the lowest frequency (22 GHz) of our observations.

respectively. The confidence intervals for the DCF values were computed using 5000 synthetic (simulated) light curves (Emmanoulopoulos et al. 2013; Connolly 2015). In this study, we found a $\sim 3\sigma$ (pre-trial) negative correlation between the 129 GHz flux density and the optical flux (Fig. 4(p)). However, this result might have been obtained by chance considering the trial factor of 33 (i.e., 500 d divided by 15 d). We used different bin sizes (7, 15, 20, 25, and 30 d) in the DCF study and found that the results were not significantly affected by bin size.

A similar cross-correlation study was performed between

a radio spectral index (α_{22-43} , α_{43-86} , or α_{86-129}) or the turnover frequency (ν_c) and the high-energy properties (α_0 , F_0 , α_X , F_X , and F_γ). The results are presented in Fig. 5. In a few pairs (e.g., Figs. 5(f) and 5(k)), we found marginally significant ($\sim 3\sigma$) correlations. However, these correlations may be insignificant considering that the trial factor is 33. Highly significant correlations were found in the $\alpha_{22-43} - F_\gamma$ ($\sim 4.5\sigma$, pre-trial) and $\alpha_c - F_\gamma$ ($\sim 4.5\sigma$, pre-trial) pairs without a time delay (Figs. 5(c) and 5(r)). These correlations are significant ($> 3\sigma$), even considering the trial factor. We verified that using different bin sizes in the DCF study did not affect the results.

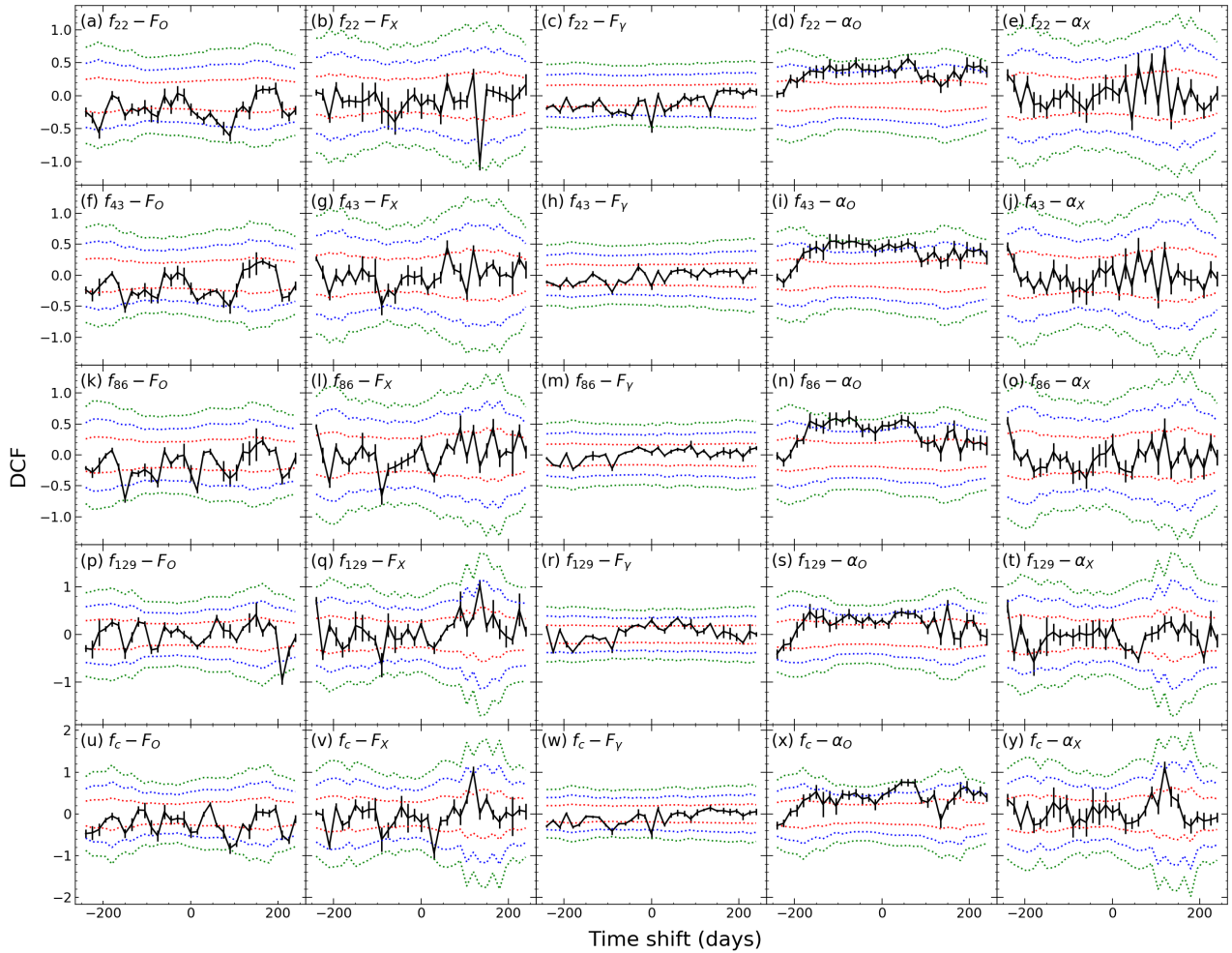


Fig. 4. Results of a DCF analysis made with the 4-band radio flux densities. Each of the 22 (f_{22} ; a-e), 43 (f_{43} ; f-j), 86 (f_{86} ; k-o), 129 GHz (f_{129} ; p-t), and turnover (f_c) flux density measurements is cross-correlated with high-energy properties: optical flux, X-ray flux, gamma-ray flux, the optical spectral index, and the X-ray index (left to right column). Red, blue, and green dotted lines are 1, 2, and 3 σ ranges for the DCF values, respectively. DCF, discrete correlation function.

4. DISCUSSION AND CONCLUSIONS

We analyzed four-band radio data obtained in contemporaneous KVN observations of 3C 279 and measured the radio spectral indices between pairs of flux density measurements. During the 5.6 year observation period, the radio flux density decreased somewhat smoothly, as observed in single-dish data taken during the same period. The low-frequency radio spectral indices (α_{22-43} and α_{43-86}) did not show significant long-term variability before MJD 57700 but started to increase after that date; the turnover frequency ν_c exhibited a similar but less significant trend. We performed a cross-correlation study and found a significant correlation between α_{22-43} and F_γ without a time delay.

We modeled the measured radio spectral energy distributions (SEDs) using a parametric model to estimate

the turnover frequency, which can provide information on SSA and thus allows us to speculate on the reasons for the radio spectral variability. Because the SSA effect is stronger at low frequencies, the SED is likely to decrease at a low frequency (the spectral turnover frequency). The measured spectral turnover frequencies for the source are between ~ 10 and ~ 40 GHz; these values are similar to the results of an earlier study (Larionov et al. 2020). Note that we have only four data points, and the highest-frequency data (129 GHz) have a very large uncertainty and thus are not very useful. Consequently, our measurements of the turnover frequency have large uncertainties, and thus its long-term variability was not clearly detected (at the 2 σ level; Section 3.1). Moreover, the ν_c values measured in some epochs lie below the lowest frequency of the KVN observations; these measurements must be interpreted cautiously.

The radio spectral changes (Figs. 2 and 3) can be

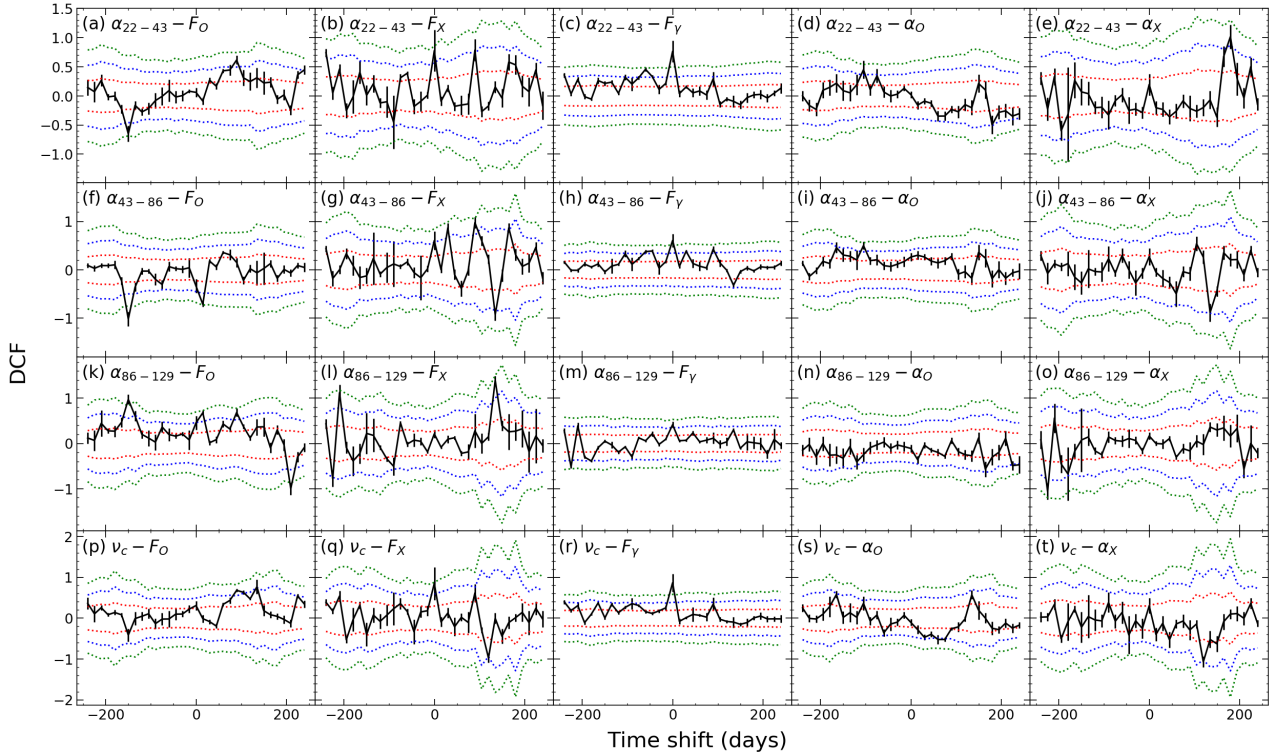


Fig. 5. Results of a cross-correlation analysis made with broadband radio spectral properties. Each of the radio spectral indices and the turnover frequency (top to bottom row) are cross-correlated with high-energy properties: optical flux, X-ray flux, gamma-ray flux, the optical spectral index, and the X-ray index (left to right column). Red, blue, and green dotted lines are 1, 2, and 3 σ ranges for the DCF values, respectively. DCF, discrete correlation function.

qualitatively understood in terms of the SSA effect in the radio-emitting region. An intrinsic (unabsorbed) power-law spectrum is observed to turn downward at the turnover frequency because the low-frequency emission is strongly absorbed. Because the lowest-frequency range, 22–43 GHz, is close to the turnover frequency (Fig. 3(d)), a change in the turnover frequency (e.g., one associated with an opacity change) due to an event in the radio-emitting region is well represented by a change in α_{22-43} , where α_{22-43} is assumed to be larger (i.e., the spectrum is harder) for higher ν_c . Thus, the hardness (spectral index) of the low-frequency emission can vary depending on the SSA opacity (which is determined by the particle number density N_e or magnetic field B). The radio spectral variability (Fig. 3) observed in the source can be explained as a result of changes in N_e or B , which are caused by activity such as particle injection or shock compression in the radio region. Weaker variability in the radio flux (weaker than that in the spectral index; compare Figs. 2(a) and 3(a)–3(b)) can also be explained by the SSA effect because the activity strengthens the radio emission, but the enhancement of the SSA effect by the activity itself simultaneously decreases it. The gradual increase in the low-frequency radio spectral indices after MJD 57700 (Figs. 3(a) and 3(b)) may suggest that particles and/or a magnetic

field B were injected into the radio-emitting region after that epoch, increasing the SSA effect.

In the extended jet scenario, the correlation and time delay between the radio and high-energy variability can provide information about the nature of the disturbance causing the variability (e.g., a shock and/or particles). Suppose that the distance between a gamma-ray region and a radio-emitting region is $d = \nu(t_2 - t_1) \equiv \nu dt$ (Fig. 6), where ν is the propagation speed of a disturbance, t_1 is an epoch of high-energy emission resulting from a disturbance at the same epoch, and t_2 is the epoch at which the disturbance arrives at the radio-emitting region. Then, the observed time delay between the two events is computed as $dt_{\text{obs}} = dt \left(1 - \frac{\nu \cos \theta_v}{c} \right)$, where c is the speed of light. Because a disturbance such as a shock cannot propagate at a speed greater than c , dt_{obs} is greater than 0; thus, a high-energy lead (i.e., radio lag) can generally be expected.

In this scenario, the contemporaneous variability (no delay, i.e., $dt_{\text{obs}} \approx 0$) of the radio and gamma-ray emission properties (the $\alpha_{22-43} - F_\gamma$ and $\alpha_c - F_\gamma$ correlations without a time delay) implies that the disturbance propagated at nearly the speed of light, and the jet viewing angle θ_v is very small. Because the θ_v value of the jet in 3C 279 is indeed very small ($\approx 3^\circ$; Hovatta et al. 2009; Liodakis et al. 2017), dt_{obs} can be approximately equal to 0 if the disturbance propagated

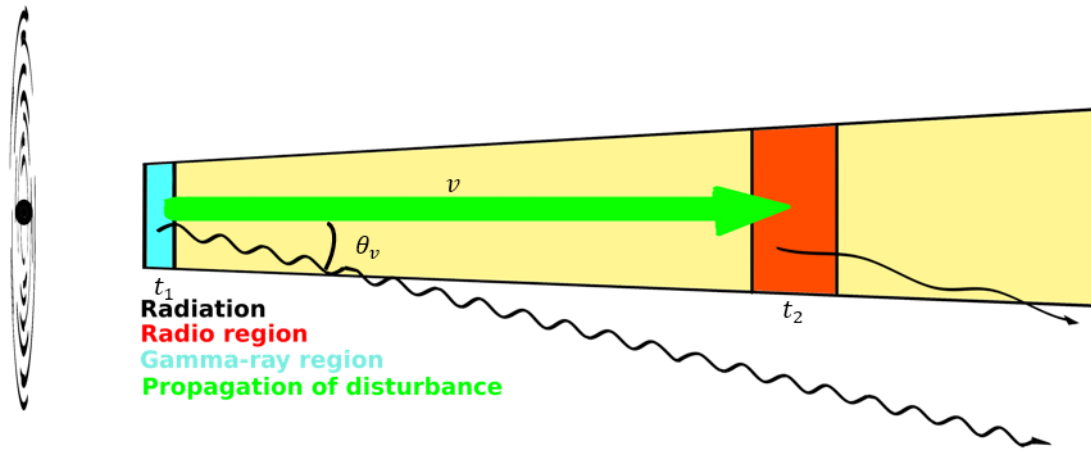


Fig. 6. A schematic view of the emission zone. A side view of the elongated jet with a high-energy region in the left (cyan) closer to the black hole (black circle) and a radio-emitting region in the right (downstream; red). The jet viewing angle is denoted by θ_v . The picture depicts a situation that a disturbance produces a gamma-ray event at t_1 in the inner region (cyan). The disturbance propagates downstream (green) to the radio region with speed v and produces a radio event at t_2 . The observed time delay between the gamma-ray and the radio radiation (curly arrows) is computed from this geometry. See text for more detail.

at the speed of light. Because a shock cannot propagate at the speed of light, we speculate that the injected particles themselves are disturbances; they produce a gamma-ray event and propagate at the speed of light ($\Gamma \sim 15$ in 3C 279; Hovatta et al. 2009; Liodakis et al. 2017) to the radio region, increasing the SSA effect (i.e., producing a hard radio spectrum). Thus, the positive correlation between α_{22-43} (or α_c) and F_r with no delay can be explained by this scenario.

Alternatively, the contemporaneous variability of the radio and gamma-ray emission may imply that the gamma-ray- and radio-emitting electrons are in the same region. However, in this case, strong SSA would prevent radio photons from leaving the emission region to approach the observer, and contemporaneous increases in the radio and gamma-ray emission are impossible. To avoid SSA, radio-emitting electrons should exist outside (low N_e and/or B) the compact gamma-ray jet. However, this scenario is not commonly used because it is unclear why the radio-emitting electrons remain in the outer envelope of the gamma-ray emission region, as radio-emitting electrons have much smaller gyro radii (e.g., $r_g \propto \frac{P_e}{B}$, where P_e is the electron momentum) than gamma-ray emitting electrons. Thus, unless there is a compelling mechanism of radio envelope formation, this scenario seems infeasible.

Note that the correlation significance we found was not very high. Furthermore, accurate flux density measurements using VLBI imaging data are challenging. Therefore, the results should be interpreted cautiously. Our conclusion awaits further confirmation, and continuing contemporaneous observations of 3C 279 will be very helpful.

ACKNOWLEDGMENTS

This research was supported by Basic Science Research Program through the National Research Foundation of Korea (NRF) funded by the Ministry of Education (2021R1A6A3A13039092). HA acknowledge supports by the Basic Science Research Program through the National Research Foundation of Korea (NRF) funded by the Ministry of Science, ICT & Future Planning (NRF-2017R1C1B2004566). SHK and SSL were supported by the National Research Foundation of Korea (NRF) grant funded by the Korea government (MIST) (2020R1A2C2009003).

ORCID

Sungmin Yoo <https://orcid.org/0000-0002-2046-4190>
 Sang-Sung Lee <https://orcid.org/0000-0002-6269-594X>
 Sang-Hyun Kim <https://orcid.org/0000-0001-7556-8504>
 Hongjun An <https://orcid.org/0000-0002-6389-9012>

REFERENCES

- Ackermann M, Ajello M, An H, Baldini L, Barbiellini G, et al., Contemporaneous broadband observations of three high-redshift BL Lac objects, *Astrophys. J.* 820, 72 (2016).
 Algaba J, Lee SS, Bindu R, Kim DW, Kino M, et al., Exploring the variability of the flat-spectrum radio source 1633+382. II. physical properties, *Astrophys. J.* 859, 128 (2018). <https://doi.org/10.1086/517111>

- org/10.3847/1538-4357/aac2e7
- An H, Romani RW, Sed constraints on the highest- z blazar jet: QSO J0906+6930, *Astrophys. J.* 856, 105 (2018). <https://doi.org/10.3847/1538-4357/aab435>
- An H, Romani RW, X-ray constraints on the spectral energy distribution of the $z = 5.18$ blazar SDSS J013127.34–032100.1, *Astrophys. J.* 904, 27 (2020). <https://doi.org/10.3847/1538-4357/abbb91>
- Blandford R, Meier D, Readhead A, Relativistic jets from active galactic nuclei, *Annu. Rev. Astron. Astrophys.* 57, 467-509 (2019). <https://doi.org/10.1146/annurev-astro-081817-051948>
- Blandford RD, Payne DG, Hydromagnetic flows from accretion discs and the production of radio jets, *Mon. Not. R. Astron. Soc.* 199, 883-903 (1982). <https://doi.org/10.1093/mnras/199.4.883>
- Blandford RD, Znajek RL, Electromagnetic extraction of energy from Kerr black holes, *Mon. Not. R. Astron. Soc.* 179, 433-456 (1977). <https://doi.org/10.1093/mnras/179.3.433>
- Connolly SD, 2015, A Python code for the Emmanoulopoulos et al. [arXiv:1305.0304], light curve simulation algorithm [Internet], viewed 2021 Feb 20, available from: <https://arxiv.org/abs/1503.06676>
- Emmanoulopoulos D, McHardy IM, Papadakis IE, Generating artificial light curves: revisited and updated, *Mon. Not. R. Astron. Soc.* 433, 907-927 (2013). <https://doi.org/10.1093/mnras/stt764>
- Fermi, 2021, 3C 279 [Internet], viewed 2021 Feb 20, available from: https://fermi.gsfc.nasa.gov/ssc/data/access/lat/msl_lc/source/3C_279
- Hayashida M, Nalewajko K, Madejski GM, Sikora M, Itoh R, et al., Rapid variability of blazar 3C 279 during flaring states in 2013–2014 with joint Fermi-LAT, NuSTAR, Swift, and ground-based multi-wavelength observations, *Astrophys. J.* 807, 79 (2015). <https://doi.org/10.1088/0004-637X/807/1/79>
- Hodgson JA, Lee SS, Zhao GY, Algaba JC, Yun Y, et al., The automatic calibration of Korean VLBI network data, *J. Korean Astron. Soc.* 49, 137-144 (2016). <https://doi.org/10.5303/JKAS.2016.49.4.137>
- Hodgson JA, Rani B, Lee SS, Algaba JC, Kino M, et al., KVN observations reveal multiple γ -ray emission regions in 3C 84? *Mon. Not. R. Astron. Soc.* 475, 368-378 (2018). <https://doi.org/10.1093/mnras/stx3041>
- Högbom JA, Aperture synthesis with a non-regular distribution of interferometer baselines, *Astron. Astrophys. Suppl.* 15, 417 (1974).
- Hovatta T, Nieppola E, Tornikoski M, Valtaoja E, Aller MF, et al., Long-term radio variability of AGN: flare characteristics, *Astron. Astrophys.* 485, 51-61 (2008). <https://doi.org/10.1051/0004-6361:200809806>
- Hovatta T, Valtaoja E, Tornikoski M, Lähteenmäki A, Doppler factors, Lorentz factors and viewing angles for quasars, BL Lacertae objects and radio galaxies, *Astron. Astrophys.* 494, 527-537 (2009). <https://doi.org/10.1051/0004-6361:200811150>
- Kiehlmann S, Savolainen T, Jorstad SG, Sokolovsky KV, Schinzel FK, et al., Polarization angle swings in blazars: the case of 3C 279, *Astron. Astrophys.* 590, A10 (2016).
- Kim JY, Krichbaum TP, Broderick AE, Wielgus M, Blackburn L, et al., Event horizon telescope imaging of the archetypal blazar 3C 279 at an extreme 20 microarcsecond resolution, *Astron. Astrophys.* 640, A69 (2020).
- Larionov VM, Jorstad SG, Marscher AP, Villata M, Raiteri CM., et al., Multiwavelength behaviour of the blazar 3C 279: decade-long study from γ -ray to radio, *Mon. Not. R. Astron. Soc.* 492, 3829-3848 (2020).
- Lee JW, Lee SS, Algaba JC, Hodgson J, Kim JY, et al., Interferometric monitoring of gamma-ray bright AGNs: OJ 287, *Astrophys. J.* 902, 104 (2020). <https://doi.org/10.3847/1538-4357/abb4e5>
- Lee S, Petrov L, Byun D, Kim J, Jung T, et al., Early science with the Korean VLBI network: evaluation of system performance, *Astron. J.* 147, 77 (2014). <https://doi.org/10.1088/0004-6256/147/4/77>
- Lee SS, Wajima K, Algaba JC, Zhao GY, Hodgson JA., et al., Interferometric monitoring of gamma-ray bright AGNs. I. the results of single-epoch multifrequency observations, *Astrophys. J. Suppl. Ser.* 227, 8 (2016). <https://doi.org/10.3847/0067-0049/227/1/8>
- Liodakis I, Marchili N, Angelakis E, Fuhrmann L, Nestoras I, et al., F-GAMMA: variability Doppler factors of blazars from multiwavelength monitoring, *Mon. Not. R. Astron. Soc.* 466, 4625-4632 (2017). <https://doi.org/10.1093/mnras/stx002>
- Lister ML, Aller MF, Aller HD, Hodge MA, Homan DC, et al., MOJAVE. XV. VLBA 15 GHz total intensity and polarization maps of 437 parsec-scale AGN jets from 1996 to 2017, *Astrophys. J. Suppl. Ser.* 234, 12 (2018). <https://doi.org/10.3847/1538-4365/aa9c44>
- Lobanov AP, Krichbaum TP, Witzel A, Zensus JA, Dual-frequency VSOP imaging of the jet in S5 0836+710, *Publ. Astron. Soc. Jpn.* 58, 253-259 (2006). <https://doi.org/10.1093/pasj/58.2.253>
- MacDonald NR, Jorstad SG, Marscher AP, “Orphan” γ -ray flares and stationary sheaths of blazar jets, *Astrophys. J.* 850, 1 (2017). <https://doi.org/10.3847/1538-4357/aa92c8>
- Marziani P, Sulentic JW, Dultzin-Hacyan D, Calvani M, Moles M, Comparative analysis of the high- and low-ionization lines in the broad-line region of active galactic nuclei, *Astrophys. J. Suppl. Ser.* 104, 37 (1996). <https://doi.org/10.1086/192291>

- Max-Moerbeck W, Richards JL, Hovatta T, Pavlidou V, Pearson TJ, et al., A method for the estimation of the significance of cross-correlations in unevenly sampled red-noise time series, *Mon. Not. R. Astron. Soc.* 445, 437-459 (2014). <https://doi.org/10.1093/mnras/stu1707>
- Murase K, Dermer CD, Takami H, Migliori G, Blazars as ultra-high-energy cosmic-ray sources: implications for TeV gamma-ray observations, *Astrophys. J.* 749, 63 (2012). <https://doi.org/10.1088/0004-637X/749/1/63>
- Rani B, Krichbaum TP, Lee SS, Sokolovsky K, Kang S, et al., Probing the gamma-ray variability in 3C 279 using broadband observations, *Mon. Not. R. Astron. Soc.* 464, 418-427 (2017). <https://doi.org/10.1093/mnras/stw2342>
- Rieger FM, Aharonian F, Probing the central black hole in M87 with gamma-rays, *Mod. Phys. Lett. A.* 27, 1230030. (2012). <https://doi.org/10.1142/S0217732312300303>
- Sokolov A, Marscher AP, Mchardy IM, Synchrotron self-compton model for rapid nonthermal flares in blazars with frequency-dependent time lags, *Astrophys. J.* 613, 725-746 (2004). <https://doi.org/10.1086/423165>
- Türler M, Courvoisier TJJ, Paltani S, Modelling 20 years of synchrotron flaring in the jet of 3C 273, *Astron. Astrophys.* 361, 850-862 (2000).
- Urry CM, Padovani P, Unified schemes for radio-loud active galactic nuclei, *Publ. Astron. Soc. Pac.* 107, 803 (1995). <https://doi.org/10.1086/133630>
- Yoo S, An H, Spectral variability of the blazar 3C 279 in the optical to X-ray band during 2009–2018, *Astrophys. J.* 902, 2 (2020). <https://doi.org/10.3847/1538-4357/abb3c1>